Appendix A Hydrodynamic model

A1 Governing equations

The governing equations are the three-dimensional, incompressible and unsteady Navier-Stokes (NS) equations written in a strong conservative form for mass and momentum. By adding the pseudo time derivate of pressure to the equation of continuity, the artificial compressibility method is used to accelerate the convergence during inner-iteration [39]. For an arbitrary deformable control volume $V(t)$, the non-dimensional governing equations are:

$$\int_{V(t)} \left(\frac{\partial \mathbf{Q}}{\partial t} + \frac{\partial \mathbf{q}}{\partial \tau} \right) dV + \int_{V(t)} \left(\frac{\partial \mathbf{F}}{\partial X} + \frac{\partial \mathbf{G}}{\partial Y} + \frac{\partial \mathbf{H}}{\partial Z} + \frac{\partial \mathbf{F}_v}{\partial X} + \frac{\partial \mathbf{G}_v}{\partial Y} + \frac{\partial \mathbf{H}_v}{\partial Z} \right) dV = 0 \tag{A1}$$

where,

$$\mathbf{Q} = \begin{bmatrix} u \\ v \\ w \\ 0 \end{bmatrix}, \mathbf{q} = \begin{bmatrix} u \\ v \\ w \\ q \end{bmatrix}, \mathbf{F} = \begin{bmatrix} u^2 + p \\ uv \\ uw \\ u\lambda \end{bmatrix}, \mathbf{G} = \begin{bmatrix} vu \\ v^2 + p \\ vw \\ v\lambda \end{bmatrix}, \mathbf{H} = \begin{bmatrix} wu \\ wv \\ w^2 + p \\ w\lambda \end{bmatrix},$$

$$\mathbf{F}_v = -\frac{1}{Re} \begin{bmatrix} 2u_X \\ u_Y + v_X \\ u_Z + w_X \\ 0 \end{bmatrix}, \mathbf{G}_v = -\frac{1}{Re} \begin{bmatrix} v_X + u_Y \\ 2v_Y \\ v_Z + w_Y \\ 0 \end{bmatrix}, \mathbf{H}_v = -\frac{1}{Re} \begin{bmatrix} w_X + u_Z \\ w_Y + v_Z \\ 2w_Z \\ 0 \end{bmatrix},$$

In the preceding equations, u, v and w are the velocity components in the Cartesian coordinate system, p is the pressure; t is the physical time and Re is the Reynolds number. The equations also contain the pseudo time parameter τ and pseudo-compressibility coefficient λ. The term q associated with pseudo time was designed for an inner-iteration at each time step, and vanished when the divergence of velocity approached zero so as to satisfy the equation of continuity. By introducing the generalized Reynolds transport theorem and by employing the Gauss integration theorem, equation (1) is transformed in a general curvilinear coordinate system as

$$\frac{\partial}{\partial t} \int_{V(t)} \mathbf{Q} dV + \int_{V(t)} \frac{\partial \mathbf{q}}{\partial \tau} dV + \int_{S(t)} (\mathbf{f} - \mathbf{Q}\mathbf{u}_g) \cdot \mathbf{n} dS = 0 \tag{A2}$$

where $\mathbf{f} = (\mathbf{F}+\mathbf{F}_v, \mathbf{G}+\mathbf{G}_v, \mathbf{H}+\mathbf{H}_v)$; $S(t)$ denotes the surface of the control volume; $\mathbf{n} = (n_X, n_Y, n_Z)$ are the components of the unit outward normal vector corresponding to all the surfaces of a polyhedral cell; $\mathbf{u}_g$ is the local velocity of the moving cell surface. For a structured, boundary-fitted, and cell-centred storage architecture, we rewrote equation (2) into a semi-discrete form:

$$\frac{\partial}{\partial t} [V\mathbf{Q}]_{ijk} + V_{ijk} \left(\frac{\partial \mathbf{q}}{\partial \tau} \right)_{ijk} + \mathbf{R}_{ijk} = 0 \tag{A3}$$

where

$$\mathbf{R}_{ijk} = (\hat{\mathbf{F}} + \hat{\mathbf{F}}_v)_{i+\frac{1}{2},j,k} - (\hat{\mathbf{F}} + \hat{\mathbf{F}}_v)_{i-\frac{1}{2},j,k} + (\hat{\mathbf{G}} + \hat{\mathbf{G}}_v)_{i,j+\frac{1}{2},k} - (\hat{\mathbf{G}} + \hat{\mathbf{G}}_v)_{i,j-\frac{1}{2},k} + (\hat{\mathbf{H}} + \hat{\mathbf{H}}_v)_{i,j,k+\frac{1}{2}} - (\hat{\mathbf{H}} + \hat{\mathbf{H}}_v)_{i,j,k-\frac{1}{2}}$$

e.g.

$$\hat{\mathbf{F}} + \hat{\mathbf{F}}_v = (\mathbf{f} - \mathbf{Q}\mathbf{u}_g) \cdot \mathbf{S}_n^{\xi}, \quad \mathbf{S}_n^{\xi} = [S_{nX}^{\xi}, S_{nY}^{\xi}, S_{nZ}^{\xi}]$$

The $(\hat{\mathbf{F}} + \hat{\mathbf{F}}_v)$ parameters refer to the two opposite surfaces *j* of a particular computational cell as indicated by the subscript +½*j* and -½*j*. The $(\hat{\mathbf{G}} + \hat{\mathbf{G}}_v)$ and $(\hat{\mathbf{H}} + \hat{\mathbf{H}}_v)$ parameters were derived in a similar manner and refer each to two opposing cell surfaces *i* and *k*. The term V_{ijk} is the volume of the cell (*i*, *j*, *k*). The superscript ξ denotes the ξ-direction perpendicular to two particular cell surfaces (indexed by *i*, while ζ-direction and η-direction are indexed by *j* and *k* respectively).

A2 Fortified solution algorithm

The geometries of the body grid and the global grid were incommensurate. It was therefore necessary to interpolate values in the overlap regions between the inter-grid boundary cells (IGBCs) and these interpolated values needed to be fortified to enhance the stability of the algorithm. The solution algorithm, which is based on a fortified NS approach [39], was derived by adding forcing terms $\sigma(\mathbf{q}_f - \mathbf{q})$ to the semi-discrete equation (3):

$$\frac{\partial}{\partial t}\left[V\mathbf{Q}\right]_{ijk} + V_{ijk}\left(\frac{\partial \mathbf{q}}{\partial \boldsymbol{\tau}}\right)_{ijk} + \mathbf{R}_{ijk} = \sigma(\mathbf{q}_f - \mathbf{q}), \tag{A4}$$

where $\mathbf{q}_f$ is derived from the interpolation (flow solution of the other overlapping grid in the last time step) in the IGBCs, and set to zero in the rest of the computational domain. In the IGBCs, the switching parameter σ was given a large positive value such that the NS equation algorithm was effectively turned off and reduced simply to $\mathbf{q}=\mathbf{q}_f$, so the solution was fortified there. In the rest of the computational domain we defined $\sigma=0$, which reduced the algorithm to the standard solution.

An implicit scheme is successively employed on equation (A4) for the physical time *t* and the pseudo-time τ for inner-iteration. Based on reasonable numerical approximations, equation (A4) could be derived into its discrete form and decomposed in sweeps in the ξ-, η- and ζ-directions. In each direction, only a linear system of equations containing a tridiagonal coefficient matrix needs to be solved, making this approach suitable for a computer-based iterative solution with comparatively low hardware requirements. More details and further derivations from equation (A4) can be found in Liu [39] and Liu and Kawachi [40].

A3 Boundary conditions

Besides the values of IGBCs obtained via the inter-grid communication, further boundary

conditions are required: 1) in the body-fitted grid, at the solid wall (surface) of the undulating body, and 2) in the global grid, at the external boundary.

On the body surface, the non-slip condition was used to define the velocity components and surface pressure in a way that accounted for dynamic effects due to the body's acceleration:

$$(u, v, w) = (u_{surface}, v_{surface}, w_{surface}),\ \partial p/\partial \mathbf{n} = -\mathbf{a}_{surface} \cdot \mathbf{n},$$

where local velocity ($u_{surface}$, $v_{surface}$, $w_{surface}$) and acceleration $\mathbf{a}_{surface}$ on the body surface are evaluated using the renewed grids in each physical step. **n** is the unit outward normal vector on body surface.

For the global grid, the boundary conditions for the velocity and the pressure were: 1) upstream (u, v, w) = 0 while pressure p was set to zero; 2) downstream and at the external boundaries of the global grid a zero-gradient condition was enforced for both velocity and pressure, i.e., $\partial(u, v, w, p)/\partial \mathbf{n} = 0$, where **n** is the unit outward normal vector at the external boundary.

A4 Validation of grid resolution

As shown in figure A2(a), the number of radial body grid layers increased with *Re*. Furthermore, the radial width of the innermost layer adjacent to the body surface was $\leqslant 0.1\ L/\sqrt{Re}$. Consequently, the radial width of a grid cell at *Re* 2 000 was three times larger than the radial width of a grid cell at *Re* 6 000. The global grid resolution followed the resolution of the body grid, ensuring that grid resolution was adjusted by *Re* in all grids. Figure A2(a) provides a kinematic validation of the grid resolution used at *Re*=6 000, the red curve shows the instantaneous force acting on the centre of mass (CoM) in the Y_{earth} direction, calculated with the grid resolution used in the manuscript (same as the *Re*=6 000 event in Figure 7 of the manuscript), while the blue curve is the same force computed with a 50% finer grid. Both grids yield very similar instantaneous force values, demonstrating that the coarser grid used in the manuscript is sufficiently fine.

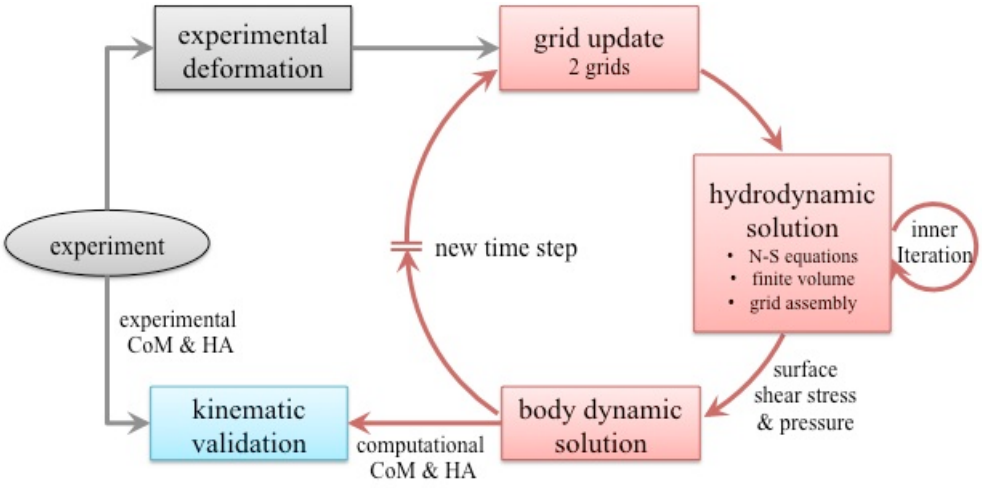

Figure A1. Overview of the numerical approach and the kinematic validation. Data from experimental observations were used as model input (body- and fin deformation) and model validation (i.e. a comparison between centre of mass (CoM) translation and heading angle obtained from experiment and model, respectively). The model consists of a numerical procedure that used prescribed time-dependent body- and fin-shapes to update the numerical grids for every time step. A finite-volume method was used to solve the Navier-Stokes equations for the fluid flow in an iterative manner for each time step, providing the solution for the external flow field as well as the shear stresses and pressures on the modelled body and fins. The force distribution on the body parts was used to compute the motion of the CoM and change in heading angle.

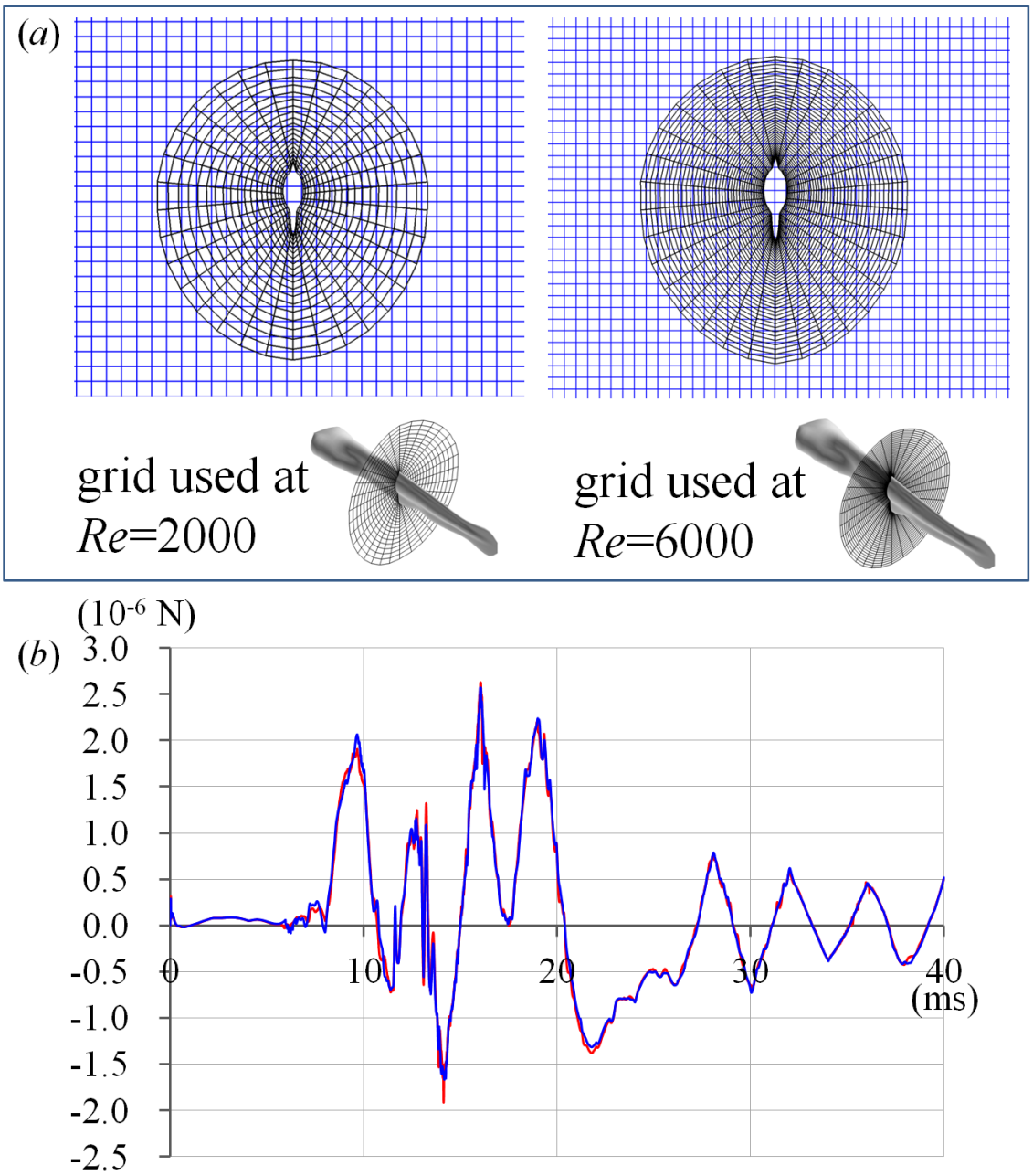

Figure A2. (*a*) body-grid (black) resolution in radial direction increased at *Re*=6 000 to ensure the radial width of the innermost layer adjacent to the body surface was $\leqslant$ 0.1 L/$\sqrt{Re}$. (*b*). Kinematic validation of the grid resolution at *Re*=6 000. Red curve: instantaneous force acting on the CoM in Y_{earth} direction at the grid resolution used in the manuscript; blue curve: force at the 50% finer grid resolution.